

# Scalar reverse-time depth migration of prestack elastic seismic data

Robert Sun<sup>○</sup> and George A. McMechan<sup>‡</sup>

## ABSTRACT

Reflected *P*-to-*P* and *P*-to-*S* converted seismic waves in a two-component elastic common-source gather generated with a *P*-wave source in a two-dimensional model can be imaged by two independent scalar reverse-time depth migrations. The inputs to migration are pure *P*- and *S*-waves that are extracted by divergence and curl calculations during (shallow) extrapolation of the elastic data recorded at the earth's surface. For both *P*-to-*P* and *P*-to-*S* converted reflected waves, the imaging time at each point is the *P*-wave traveltimes from the source to that point. The extracted *P*-wave is reverse-time extrapolated and imaged with a *P*-velocity model, using a finite difference solution of the scalar wave equation. The extracted *S*-wave is reverse-time extrapolated and imaged similarly, but with an *S*-velocity model. Converted *S*-wave data requires a polarity correction prior to migration to ensure constructive interference between data from adjacent sources. Synthetic examples show that the algorithm gives satisfactory results for laterally inhomogeneous models.

## INTRODUCTION

In conventional two-dimensional (2-D) reflection seismic exploration, it is ideal if the acquired seismic reflection data contain only *P*-waves or only *S*-waves. For a *P*-wave source, vertical geophones record predominantly *P*-waves and in-line horizontal geophones record predominantly *P*-to-*S* converted waves. As the ray path of the emerging reflected wave is usually not absolutely vertical, reflected *P*-waves have some horizontal component and reflected *S*-waves have some vertical component; the amount of mixing is angle dependent. Some *S*-wave energy will be recorded by vertical geophones and some *P*-wave energy will be recorded by horizontal geophones.

However, there is clearly some advantage to independent imaging of both *P*- and *S*-waves, as they provide more information together than either does alone.

Kirchhoff elastic wave migration has been implemented by Kuo and Dai (1984) and by Dai and Kuo (1986). Elastic reverse-time migration has been implemented by Sun and McMechan (1986) and Chang and McMechan (1987) using two-component (in-line and vertical) synthetic data, and by Chang and McMechan (1994) using 3-D synthetic data. In these algorithms, the coupled *P*-to-*P* and *P*-to-*S* converted reflections are imaged by extrapolation of the multicomponent wavefields using accurate *P*- and *S*-velocities in an elastic model using the elastic wave equation.

Sun (1999) presented preliminary results of the approach to separate *P*- and *S*-waves in elastic data that is used in this paper. The wavefield separation is implemented with divergence and curl calculations that involve spatial derivatives; thus, a  $\phi/2$  phase shift is induced. Sun et al. (2001) developed an algorithm to correct the phase in the separated *P*- and *S*-waves by imposing a compensating  $\phi/2$  phase shift. Migrating the *P*-to-*P* and *P*-to-*S* converted reflections independently thus becomes possible. After the separation, the *P*- and converted *S*-wavefields are independently input as reverse-time boundary conditions to separate scalar reverse-time depth migrations (McMechan, 1983; Chang and McMechan, 1987; Mufti et al., 1996). The *P*-wave can be imaged using a *P*-velocity model for data extrapolation, and the *S*-wave can be imaged using an *S*-velocity model. The coupling between *P*- and *S*-waves, and the resulting converted wave artifacts in the images that are present in elastic extrapolation, are therefore avoided.

This paper deals only with synthetic elastic data; application to real data is left for future research. We first illustrate the algorithm with a simple laterally homogeneous model with two horizontal reflectors. Then, we test the algorithm with a (vertically and laterally) inhomogeneous model containing reflectors of progressively increasing dip angles. Finally, we illustrate the effect of using incorrect velocities and of lateral inhomogeneity in the near surface on the migration.

Manuscript received by the Editor June 24, 1999; revised manuscript received August 3, 2000.

<sup>○</sup>National Chengkung University, Department of Earth Sciences, 1 Tahsueh Road, Tainan, Taiwan 701, Taiwan, ROC. E-mail: sun@geotech. ncku.edu.tw.

<sup>‡</sup>University of Texas at Dallas, Center for Lithospheric Studies, P.O. Box 830688, Richardson, Texas 75083-0688. E-mail: mcmec@utdallas.edu.

© 2001 Society of Exploration Geophysicists. All rights reserved.

## METHODOLOGY

Both elastic and scalar wave propagations are involved in this algorithm (for modeling, for  $P$ - $S$  wave separation, and for migration). In isotropic media, the two coupled equations involved in 2-D elastic wave extrapolation in rectangular  $(x, z)$  coordinates are (Kelly et al., 1976; Sun and McMechan, 1986)

$$\frac{\partial^2 u}{\partial t^2} = \phi^2 \frac{\partial^2 u}{\partial x^2} + (\phi^2 \circ \phi^2) \frac{\partial^2 w}{\partial x \partial z} + \phi^2 \frac{\partial^2 u}{\partial z^2} \quad (1a)$$

and

$$\frac{\partial^2 w}{\partial t^2} = \phi^2 \frac{\partial^2 w}{\partial z^2} + (\phi^2 \circ \phi^2) \frac{\partial^2 u}{\partial z \partial x} + \phi^2 \frac{\partial^2 w}{\partial x^2}, \quad (1b)$$

where  $t$  is time,  $u(x, z, t)$  and  $w(x, z, t)$  are the horizontal and vertical (particle displacement or velocity) response components, respectively, and  $\phi$  and  $\phi$  are the  $P$ - and  $S$ -wave velocities, respectively. The two-dimensional scalar wave equation is

$$\frac{\partial^2 Q}{\partial t^2} = c^2 \left( \frac{\partial^2 Q}{\partial x^2} + \frac{\partial^2 Q}{\partial z^2} \right), \quad (2)$$

where  $Q(x, z, t)$  is the scalar wave function and  $c$  is the wave velocity. In both equations (1) and (2), density is assumed to be constant, the  $x$ -coordinate (horizontal position) increases to the right, and the  $z$ -coordinate (depth) increases downward from the free surface.

Finite difference simulations of fourth-order accuracy in spatial derivatives and second-order accuracy in time derivatives (Dablain, 1986) of the wave equations (1) and (2) are used in the wave extrapolations. The grid spacing  $h = 0.01$  km in both  $x$ - and  $z$ -coordinates, the time sampling increment  $\Delta t = 0.001$  s, and a dominant source frequency of 16 Hz are used throughout this paper.

A simple laterally homogenous model of 4.0 km horizontal extent and 2.5 km depth extent (Figure 1) is used to illustrate the algorithm. This model simulates a vertical plane through a medium with two horizontal reflectors with its top at the earth's free surface. A  $P$ -wave source is located at  $(x, z) = (2.0, 0.14)$  km. The synthetic (two-component) data for receivers at the top of the grid, computed using the elastic wave equa-

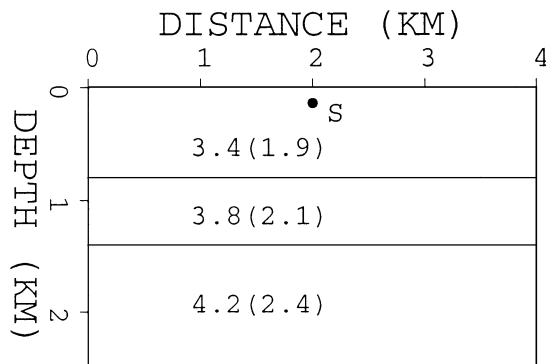


FIG. 1. A 2-D elastic model with two horizontal reflectors. The elastic common-source data generated from this model (Figure 2) are used to illustrate the algorithm. The numbers outside the parentheses are  $P$ -velocities, and the numbers inside the parentheses are  $S$ -velocities (all in km/s). Receivers are along the top of the model. S denotes a source location.

tion (1), are shown in Figures 2a and 2b. After removing the surface waves by an  $f$ - $k$  filter and muting the direct arrivals, the reflected  $P$ -to- $P$  and  $P$ -to- $S$  converted waves are shown in Figures 2c and 2d. Surface waves can also be removed during reverse-time extrapolation (McMechan and Sun, 1991; Sun and McMechan, 1991), but this requires extrapolation to a greater depth than  $P$ - $S$  wave separation.

The approach in this paper is to extract  $P$ - and  $S$ -waves from the elastic data (Figures 2c and 2d) and then to perform scalar reverse-time depth migrations separately on the  $P$ - and  $S$ -wave data. For  $P$ - and  $S$ -wave extractions, we propose two methods as described below. In method I, we do elastic downward continuation of the surface data,  $P$ - $S$  wave separation by divergence and curl calculations at a predefined datum, followed by independent scalar finite difference upward continuations of the  $P$ - and  $S$ -waves back to the surface, where they are input to separate scalar wave-equation migrations. Method II is similar, but the final migrations are performed directly from the datum at which the wave separation is performed rather than from the free surface. The extrapolation of the recorded wavefield for  $P$ - $S$  wave separation is independent of the source

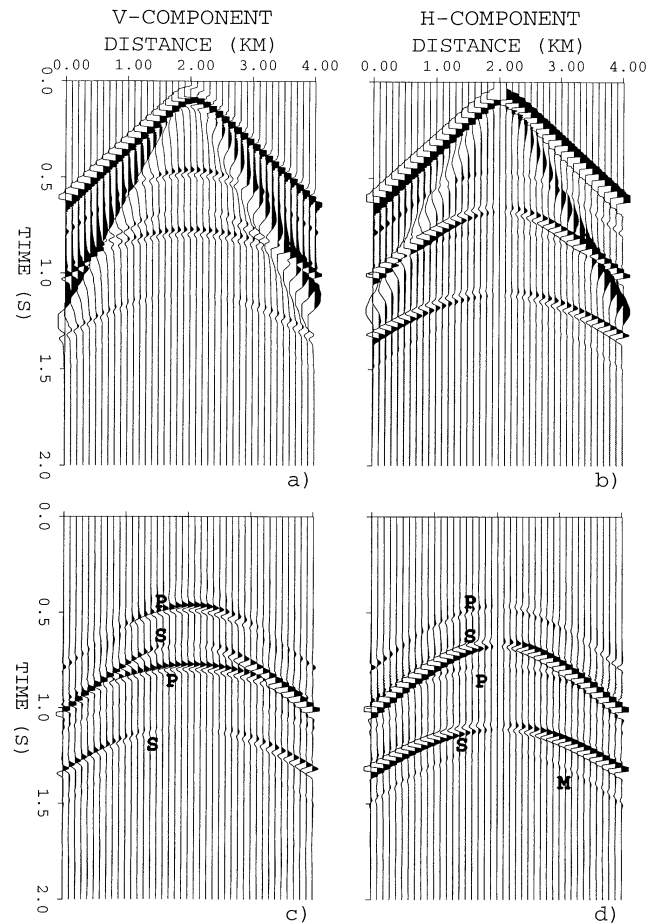


FIG. 2. Vertical (a) and horizontal (b) components of the synthetic common-source elastic data for the model in Figure 1. Vertical (c) and horizontal (d) components of the elastic data after removing the direct arrivals and surface waves. P denotes the  $P$ -to- $P$  reflections, and S denotes the  $P$ -to- $S$  converted reflections. The energy M is an interlayer multiple. The amplitudes in (a) and (b) have been weighted by a factor of 0.5.

location; for a deep source, the datum at which the separation is performed may be above or below the source depth.

### Method I: Reconstructing pure *P*- and converted *S*-waves at the earth's surface

This method applies *P*-*S* wave separation (Sun, 1999) before scalar reverse-time depth migration. The two-component elastic common-source data (Figures 2c and 2d) are extrapolated in reverse time with a vertically homogeneous elastic model (to avoid artifacts generated by near-surface reflection or conversion). The dilatation (the divergence of the wavefield)

$$\phi = \frac{\partial u}{\partial x} + \frac{\partial w}{\partial z} \quad (3a)$$

(representing pure *P*-waves) and the rotation (the curl of the wavefield)

$$\phi = \frac{\partial u}{\partial z} - \frac{\partial w}{\partial x} \quad (3b)$$

(representing pure *S*-waves) are calculated at some shallow depth  $z_1$  (here, we use  $z_1 = 0.1$  km). Two upward scalar extrapolations (one for the *P*-wave data and the other for the *S*-wave data) are then performed using equation (2) to obtain the separated *P*- and *S*-wavefields back at the earth's surface. After phase correction (Sun et al., 2001), the *P*- and *S*-wave data

(Figures 3a and 3b) are each input to scalar reverse-time depth migrations.

For migration, two velocity models, one with the *P*-velocity (Figure 1) and the other with the *S*-velocity (Figure 1), are prepared. The velocity distributions have been smoothed to reduce reflection at the reflectors (and thus to reduce migration artifacts) during the wave propagation computation (Loewenthal et al., 1987). The imaging time at each grid point for both *P*-to-*P* and *P*-to-*S* converted reflections is the one-way *P*-wave traveltide from the source when *P*-wave sources are used. This assumes that all the reflected *S*-waves are generated exclusively by *P*-to-*S* conversion. The imaging time is determined using ray tracing in the *P*-velocity model. The use of ray tracing for computing the imaging time is efficient, but also may produce some ambiguities in complicated structures where there may be multiple paths between the source and some image points (Geoltrain and Brac, 1993).

The *P*-wave data (Figure 3a) are reverse-time extrapolated into the *P*-velocity model (Figure 1) using the scalar wave equation (2) with  $Q$  set to the *P*-wave amplitude (the divergence  $\phi$ ) and  $c$  set to the *P*-wave velocity  $\phi$ . During reverse-time extrapolation, the *P*-image at each point (Figure 4a) is extracted as the *P*-wave amplitude at the image time at that point. The separated *S*-wave data (Figure 3b) are reverse-time extrapolated into the *S*-velocity model (Figure 1) again with the scalar wave

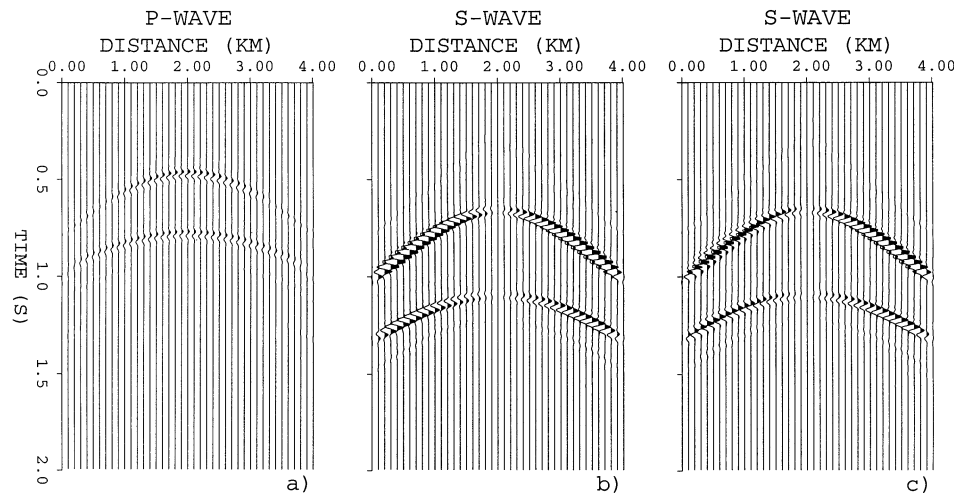


FIG. 3. The *P*-waves (a) and *S*-waves (b), extracted from the elastic data in Figures 2c and 2d, as reconstructed at the earth's surface. (c) is the polarity corrected version of the *S*-wave data in (b). Compare (a) and (c) with the input (unseparated) wavefields in Figures 2c and 2d. The spatial aperture edges of the data are tapered to reduce edge artifacts during migration.

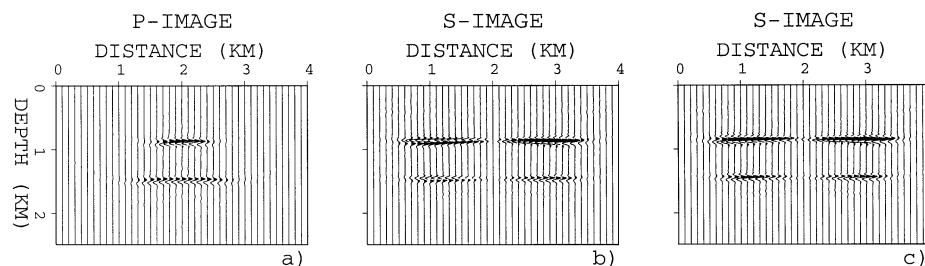


FIG. 4. The migrated *P*-image (a), *S*-image (b), and polarity-corrected *S*-image (c) of the elastic data in Figure 2 using method I. The *S*-images have been weighted by a factor of 0.5 to make the amplitudes in (a), (b), and (c) comparable; see discussion in the text.

equation (2), with  $Q$  set to the  $S$ -wave amplitude (the curl  $\phi$ ) and  $c$  equal to the  $S$ -velocity  $\phi$ . During reverse-time extrapolation, the  $S$ -image at each point (Figure 4b) is extracted as the  $S$ -wave amplitude at the imaging time of that point. The  $S$ -wavefield is the curl vector  $\phi$  which, for 2-D propagation, has only one component, which is perpendicular to the plane of propagation for  $SV$  displacement in the plane (Grant and West, 1965; Sheriff and Geldart, 1982). This one decoupled component  $\phi$  can be extrapolated by the scalar equation (2) in the same way that an  $SH$ -wave (which has displacements perpendicular to the propagation plane) can be propagated with a 2-D scalar wave equation (Kelly, 1983). We use the terms  $P$ -image and  $S$ -image to mean migrated images produced by primary  $P$ -to- $P$  reflections and  $P$ -to- $S$  converted reflections, respectively.

Comparing Figures 4a and 4b with the original model (Figure 1), we see that both the reflected  $P$ - and  $S$ -waves are accurately imaged at the reflectors with only minor artifacts. Along a reflector, the amplitudes of both  $P$ - and  $S$ -images are location dependent. Also the energy distributions in the  $P$ - and  $S$ -images are different. For an incident  $P$ -wave, the  $P$ -wave and converted  $S$ -wave reflections have different reflection angles and different angle-dependent reflection coefficients (e.g., Aki and Richards, 1980, 133–152).

Since the pure  $P$ - and  $S$ -waves are represented by different physical quantities (divergence and curl, respectively), and they respond to different elastic properties, they may show very different amplitudes; therefore, a weighting factor may be helpful for balancing the amplitudes for plotting. A polarity reversal is presented in the  $S$ -wave to either side of the source in both the input  $S$ -wave data (Figure 3b) and in the corresponding migrated image (Figure 4b) because of the vector polarization inherent in the  $S$ -wave. This produces destructive interference when the  $S$ -wave images are stacked over shots. Thus a polarity correction (see Appendix A) is applied to the  $S$ -waves (Figure 3b) before migration. The result is shown in Figure 3c. The data in Figure 3c are reverse-time depth migrated to get the polarity-corrected  $P$ -to- $S$  converted wave image in Figure 4c. Note that this polarity correction cannot be done prior to  $P$ - $S$  wave separation as it is applicable only to the  $S$ -waves; thus, this is a key limitation to the use of elastic extrapolation of multicomponent data in migration (for example in elastic reverse-time migration).

#### Method II: Extracting pure $P$ - and $S$ -waves at a shallow datum

With this method, elastic reverse-time extrapolation is performed to a new datum near the top of the finite difference grid, and scalar reverse-time extrapolation is performed downward from that datum. To perform the elastic extrapolation, an elastic velocity model with near-surface  $P$ - and  $S$ -velocities is constructed (Figure 5). The two-component elastic data (Figure 2) are reverse-time extrapolated from the receiver locations (at the earth's surface) into the elastic model using the elastic wave equations (1) to some (shallow) depth  $z_1$  (here, we use  $z_1 = 0.1$  km, denoted by the dashed line in Figure 5). Separated  $P$ -waves (the divergence  $\phi$ ) and  $S$ -waves (the curl  $\phi$ ) are extracted using equations (3a) and (3b) at depth  $z_1$ . After correcting the  $\phi/2$  phase shift (Sun et al., 2001) and correcting the  $S$ -wave polarity (Appendix A), the separated  $P$ - and  $S$ -waves are shown in Figures 6a and 6b. To have sufficient grid points

for fourth-order finite differences of the derivatives in equations (3a) and (3b), we should have  $z_1 \geq 2h$  since a total of five grid points are needed in the  $z$ -direction.

For migration, scalar reverse-time extrapolation is performed from  $z_1$  to depths below  $z_1$ , following the same procedure described above for method I. The resulting  $P$ -image is shown in Figure 7a, and the resulting  $P$ -to- $S$  converted wave image is shown in Figure 7b. The results of method I (Figures 4a and 4c) and method II (Figures 7a and 7b) are virtually the same; both results accurately image the original model (Figure 1).

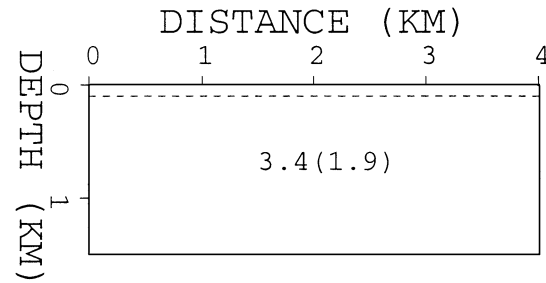


FIG. 5. Elastic velocity model for elastic reverse-time extrapolation. The top boundary represents the earth's surface. The dashed line is at depth  $z_1 (=0.1$  km) where the divergence and curl are calculated and where reverse-time extrapolation switches from one elastic extrapolation to two scalar ( $P$  and  $S$ ) extrapolations. The number outside the parentheses is the  $P$ -velocity, and the number inside the parentheses is the  $S$ -velocity all in km/s.

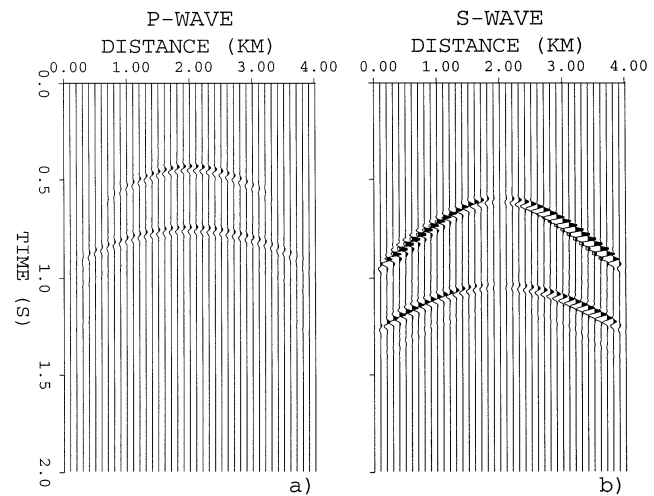


FIG. 6. The  $P$ -waves (a) and  $S$ -waves (b) extracted from the elastic data in Figure 2 at depth  $z_1 = 0.1$  km. The  $S$ -waves are polarity corrected.

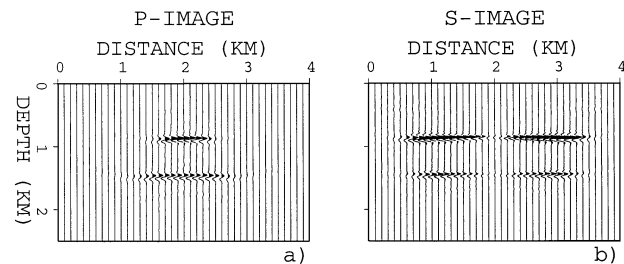


FIG. 7. The migrated  $P$ -image (a) and  $S$ -image (b) of the elastic data in Figure 2 using method II. The  $S$ -image has been weighted by a factor of 0.5.

### A LATERALLY INHOMOGENEOUS EXAMPLE

The migration algorithm is further tested using a laterally inhomogeneous elastic model containing reflectors with progressively increasing dip angles (Figure 8). Figures 9a and 9b show the synthetic elastic data generated with a  $P$ -wave source at  $(x, z) = (1.5, 0.14)$  km ( $S_3$  in Figure 8) and with absorbing boundaries on all four edges. Figures 9c and 9d show the synthetic elastic data generated with a  $P$ -wave source at  $(3.0, 0.14)$  km ( $S_6$  in Figure 8). In Figure 9, the direct arrivals have been muted.

Method II is used to perform scalar reverse-time depth migrations.  $P$ - and  $S$ -waves are extracted at depth  $z_1 = 0.1$  km, the  $\phi/2$  phase shift induced in  $P$ - $S$  wave separation (Sun et al., 2001), and the polarity in the  $S$ -waves are corrected (Appendix A). Note that the polarity correction must be done after the  $P$ - $S$  wave separation (because only the  $S$ -wave is involved) and before migration [because the null position is always near zero offset in a common source gather before migration, but moves in a dip-dependent (and hence difficult to generalize) fashion during migration]. The separated  $P$ - and  $S$ -waves for the source  $S_3$  are shown in Figures 10a and 10b, respectively, and those for the source  $S_6$  are shown in Figures 10c and 10d, respectively. The migrated  $P$ - and  $S$ -images for the source  $S_3$  are shown in Figures 11a and 11b, respectively. The migrated  $P$ - and  $S$ -images for the source  $S_6$  are shown in Figures 11c and 11d, respectively. Figures 11e and 11f contain the stacks over the images from sources  $S_1$  through  $S_7$ .

### EFFECT OF INCORRECT VELOCITIES AND LATERAL INHOMOGENEITY IN THE NEAR SURFACE

All the examples presented above have laterally homogeneous velocities in the near surface, and use correct velocities for  $P$ - $S$  wave separation. Next, we demonstrate that this is not a requirement. Figure 12a is a laterally inhomogeneous elastic model that is modified from Figure 1. The synthetic elastic data generated with a  $P$ -wave source at point S and recorded at the top of the grid, after removing the direct arrivals and surface waves, are shown in Figures 13a and 13b. Figure 12b shows a laterally homogeneous velocity model, with about 5% deviations

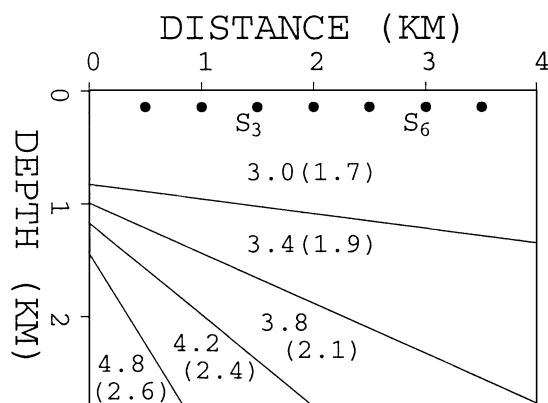


FIG. 8. A laterally inhomogeneous model. The numbers outside the parentheses denote  $P$ -velocities, and the numbers inside the parentheses denote  $S$ -velocities (all in km/s). The dots denote  $P$ -wave source locations at  $(x, z)$  with  $x$  from 0.5 to 3.5 km at 0.5 km increment and  $z = 0.14$  km.

from the correct velocities used for  $P$ - $S$  wave separation. The separated  $P$ - and  $S$ -waves extracted at the top of the model using method I, after phase correction, are shown in Figures 13c and 13d, respectively. The consistency in arrival times of the separated waves implies that the effect of the velocity errors is not significant; downward followed by upward extrapolation through any smooth velocity model is reversible. The migrated  $P$ - and  $S$ -images, using correct  $P$ - and  $S$ -velocities, are presented in Figures 14a and 14b, respectively. Both  $P$ - and  $S$ -waves are correctly imaged at the reflectors even though they were separated using approximate velocities.

When method II is employed, the accuracy of the near-surface velocity model through which extrapolation is done is more important than for method I; the initial extrapolation for  $P$ - $S$  wave separation is also the first part of the migration. A less accurate velocity model may be acceptable if the depth at which the  $P$ - $S$  wave separation is done is very shallow.

### DISCUSSION AND CONCLUSIONS

As separating  $P$ - and  $S$ -waves in elastic seismic data becomes possible, it is natural to use pure  $P$ - and  $S$ -waves to produce

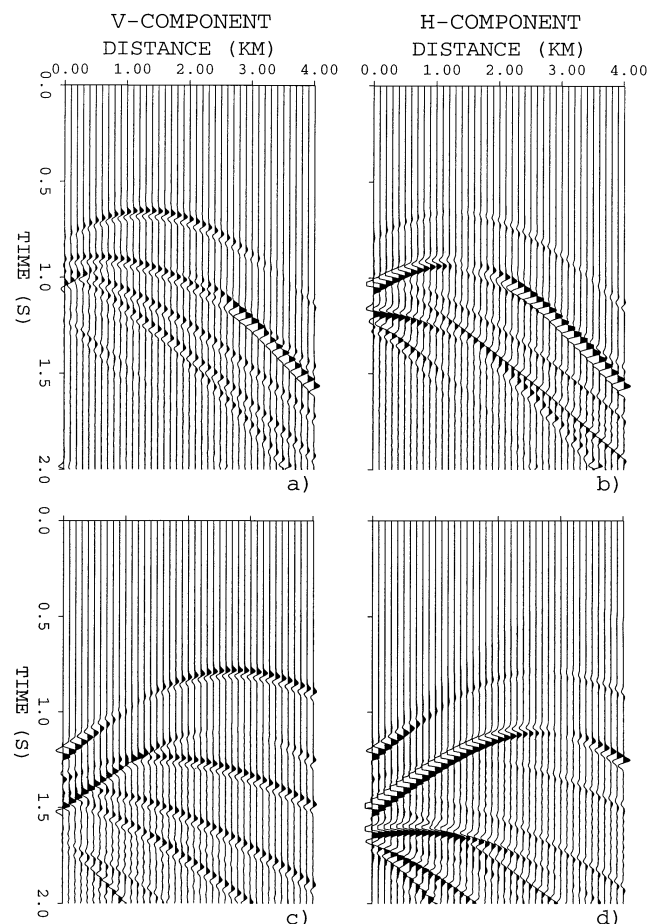


FIG. 9. Synthetic elastic common-source data generated for the model in Figure 8. Vertical (a) and horizontal (b) components generated with a  $P$ -wave source  $S_3$  at  $(x, z) = (1.5, 0.14)$  km; vertical (c) and horizontal (d) components generated with a  $P$ -wave source  $S_6$  at  $(x, z) = (3.0, 0.14)$  km. The direct arrivals have been muted.

independent images and stacks over common-source images. Synthetic examples demonstrate that the  $P$ - and  $S$ -waves in elastic data can be separated and then imaged independently by scalar reverse-time depth migration. Correcting the  $S$ -image polarity reversal is necessary, which would be difficult if  $P$ - and  $S$ -waves were not separated. Elastic reverse-time migration (Sun and McMechan, 1986; Chang and McMechan, 1987), for example, will provide an image that is the sum of the images computed directly from the coupled  $P$ - and  $S$ -waves in the elastic data, but is unable to handle the  $S$ -wave polarity reversal properly.

Extrapolation during the  $P$ - $S$  wave separation and migration is performed with the elastic reverse-time boundary condition. The recording at the free surface contains the superposition of both upgoing and downgoing waves. This free surface response will be fully reproduced by the boundary conditions in the extrapolations for  $P$ - $S$  wave separation and migration. Use of displacement components and the reverse-time boundary condition is sufficient for migration. However, if staggered grid formulation is used, the boundary condition for the stress tensor should be implemented using a band-limited spatial delta

function and a band-limited first-order derivative of the spatial delta function (Mittet, 1994).

The input data are tapered at the maximum-time edge before extrapolation to ensure stability. There is an implicit data gradient because the data changes from zero amplitude at the last data point to a finite value at the next to last point. As soon as a few time slices have been inserted as boundary conditions and the data amplitudes begin to ramp up, all derivatives and the data gradient needed to predict the interior field are obtained from the propagating wavefield in the grid and the data values being extrapolated.

In this paper, we only present synthetic examples that assume correct relative amplitudes of the different vector components. In real data processing, we will have to obtain correct relative amplitudes of the components. This preprocessing problem will be encountered in all  $P$ - $S$  wave separation algorithms; it is not unique to the approach illustrated here. Similarly, the scalar migration approach can be applied to separated  $P$ - and  $S$ -wave data, regardless of how the separation is done.

For a  $P$ -wave incident at a reflector, the reflection angles for the reflected  $P$ - and  $S$ -waves are different (by Snell's law). The reflected  $P$ - and  $S$ -waves received at the same surface location have different reflecting points even when the reflector is a plane, and will therefore be imaged at different subsurface locations (Figure A-1). Using both the  $P$ - and  $S$ -waves extracted from elastic data, therefore, provides information about different locations on a reflector.

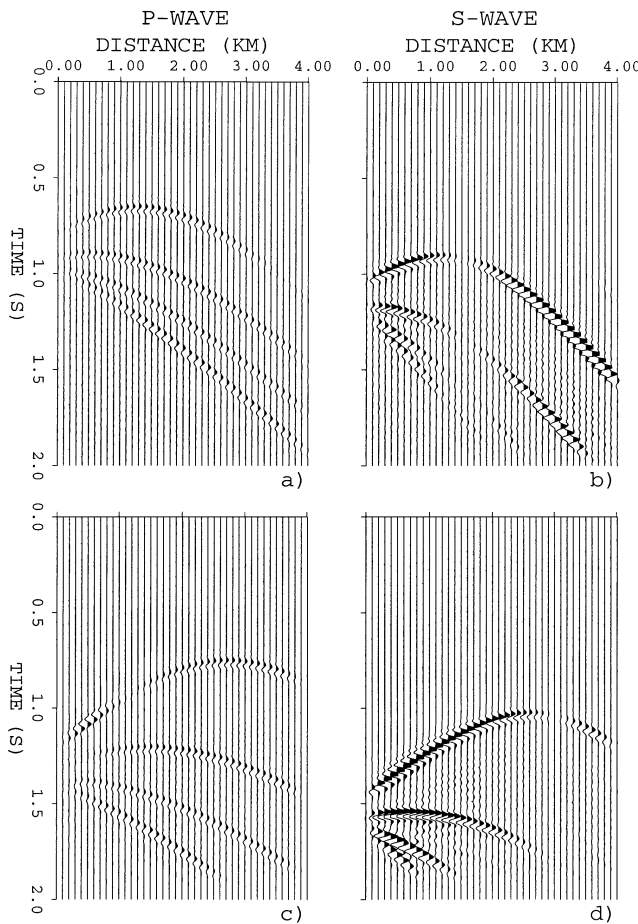


FIG. 10. The  $P$ -waves (a) and  $S$ -waves (b) are extracted from the elastic data in Figures 9a and 9b. The  $P$ -waves (c) and  $S$ -waves (d) are extracted from the elastic data in Figures 9c and 9d. The  $P$ -waves with negative reflection coefficient at large offsets are muted before migration; this polarity change corresponds to a class 1 amplitude-variation-with-offset anomaly (Rutherford and Williams, 1989).

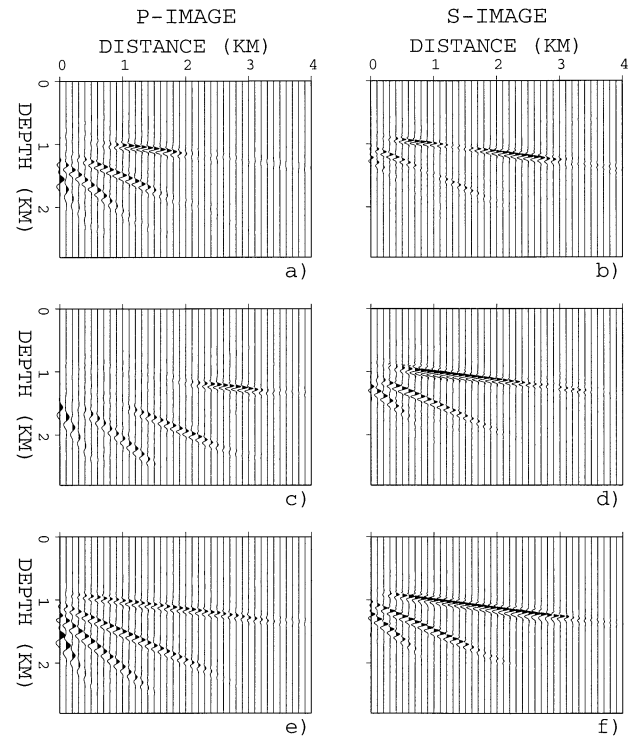


FIG. 11. Separated  $P$ - and  $S$ -images using method II. (a) and (b) contain the  $P$ - and  $S$ -images, respectively, of the elastic data (Figures 9a and 9b) for a source at  $x = 1.5$  km. (c) and (d) contain the  $P$ - and  $S$ -images, respectively, of the elastic data (Figures 9c and 9d) for a source at  $x = 3.0$  km. (e) and (f) contain the normalized sums of the images from all seven sources whose locations are shown in Figure 8. All the  $S$ -images have been weighted by a factor of 0.5.

*S*-wave exploration, using *S*-waves from *S*-sources, provides a tool that complements *P*-wave exploration. We demonstrated here that the *P*-to-*S* converted waves (rather than the *S*-waves generated with an *S*-source) can be used for *S*-wave exploration as well. *S*-sources are more difficult to generate and tend to be less pure than *P*-sources. Acquiring data with a *P*-source is much easier and cheaper than with an *S*-source. In principle, the procedures described above are also directly applicable to data from *S*-wave sources; the main difference is that an *S*-wave velocity model would be used to compute the image condition in migration, and the separated data would contain *S*-*S* reflections and *S*-*P* conversions.

The prestack migrated images can be stacked with various combinations depending on the purpose. Stacking *P*-images over sources will provide information about *P*-to-*P* reflectivity. Stacking *S*-images over sources will provide information about *P*-to-*S* conversion reflectivity. Stacking the *P*- and *S*-images together is possible, but this mix loses physical interpretability and, if not accurate, the *P*- and *S*-images may not be added coherently. The resolution of the *P*- and *S*-images may also be difference because of differences in absorption.

Two migration methods are presented in this paper. Method I performs the *P*-*S* wave separation and reconstructs pure *P*- and *S*-waves at the earth's surface. The separated *P*- and *S*-waves (e.g., Figure 3) have the same arrival times as in the original elastic data (e.g., Figure 2) because the downward and upward continuations use the same *P*- and *S*-velocities. Method II in-

volves elastic reverse-time extrapolation into the near surface and then switches to scalar extrapolation at some depth. The *P*- and *S*-waves at this depth will have different arrival times than those in the original elastic data because the wavefields have been downward continued to a new datum, but will still satisfy the same imaging time, which is determined by ray tracing from the source. Both methods give satisfactory migration outputs.

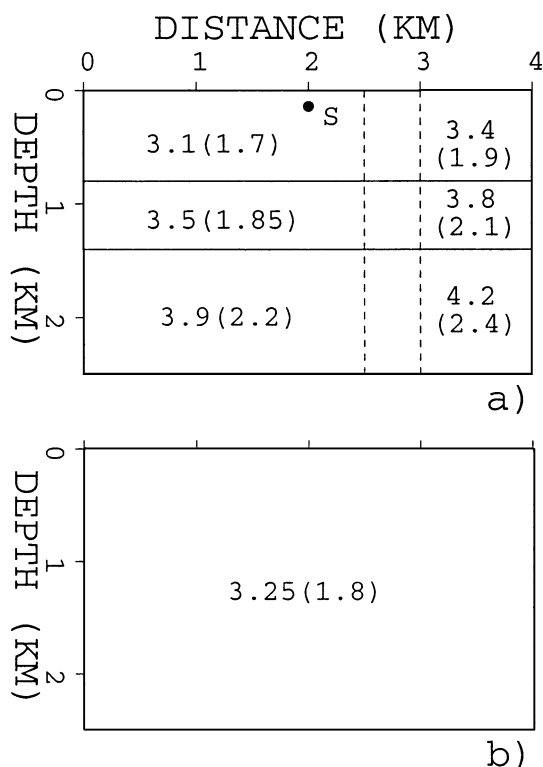


FIG. 12. (a) A 2-D elastic model, modified from Figure 1, with laterally inhomogeneous velocities in the near surface, and (b) the (incorrect) homogeneous elastic velocity model used for *P*-*S* wave separation. The numbers outside the parentheses are *P*-velocities, and the numbers inside the parentheses are *S*-velocities (all in km/s). The region between the two vertical dashed lines has horizontally linearly interpolated velocities. *S* denotes a source location.

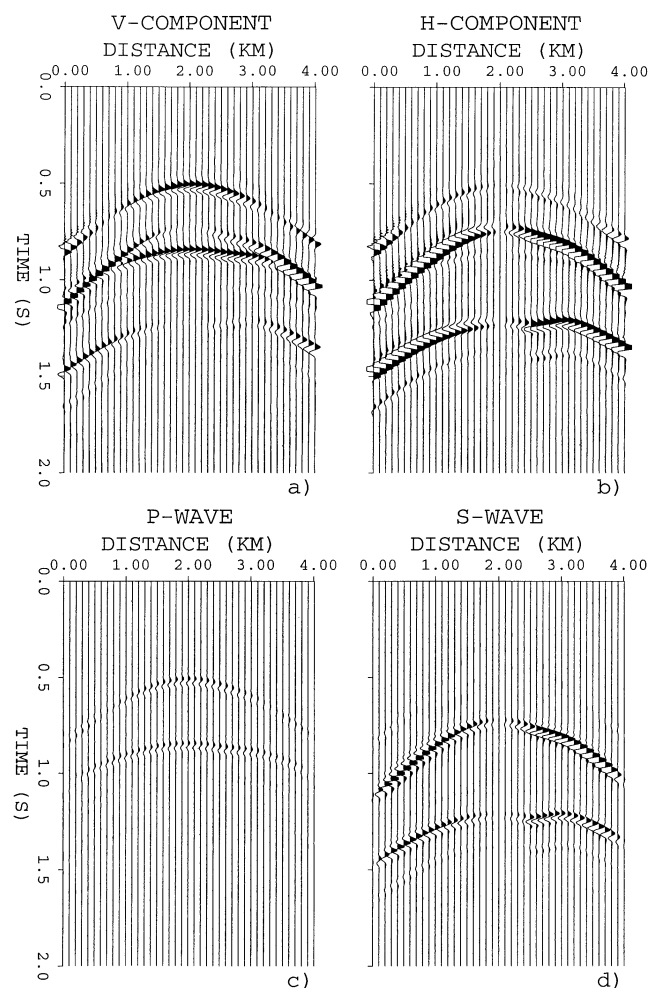


FIG. 13. Vertical (a) and horizontal (b) components of the synthetic common-source elastic data for the laterally inhomogeneous model in Figure 12, after removing the direct arrivals and surface waves. *P*-waves (c) and *S*-waves (d) (after polarity correction) are extracted from the elastic data in (a) and (b), as reconstructed at the earth's surface.

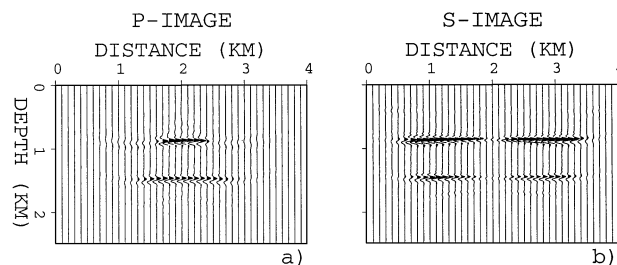


FIG. 14. The migrated *P*-image (a), and *S*-image (b) of the elastic data in Figure 13 using method I. Compare with Figure 7.

In the examples, the  $P$ -to- $S$  converted reflection amplitudes are larger than the primary  $P$ -wave reflections because of the combination of two effects. First, the  $P$ -to- $S$  conversion is especially efficient at the sharp (and large) velocity contrast in the model. Second, the shear modulus is smaller than the compressional modulus by about a factor of two, so all else being equal, the shear amplitudes will normally be larger than the compressional amplitudes by a factor of two. However, in the presence of attenuation, the  $S$ -waves tend to decay more quickly.

Processing one prestack, common-source, two-component record of 400 receivers and 2000 time samples, in a computational grid of 400 by 250 points, takes about 60 s CPU time on 2 nodes in an IBM SP2 parallel processor.

#### ACKNOWLEDGMENTS

We are grateful to Dr. Dan Whitmore, Dr. Ketil Hokstad, and two anonymous reviewers for their constructive comments. The computations in this research were done at the National Center for High-Performance Computing (NCHC) in Taiwan. The research leading to this paper was funded by the National Science Council of Taiwan under grant no. NSC88-2116-M-006-017.

#### REFERENCES

- Aki, K., and Richards, P. G., 1980, Quantitative seismology: W. H. Freeman & Co.
- Balch, A. H., and Erdemir, C., 1994, Sign-change correction for prestack migration of  $P$ - $S$  converted wave reflections: *Geophys. Prosp.*, **42**, 637–663.
- Chang, W. F., and McMechan, G. A., 1987, Elastic reverse-time migration: *Geophysics*, **52**, 1365–1375.
- , 1994, 3-D elastic prestack reverse-time depth migration: *Geophysics*, **59**, 597–609.
- Dablain, M. A., 1986, The application of high-order differencing to the scalar wave equation: *Geophysics*, **51**, 54–66.
- Dai, T. F., and Kuo, J. T., 1986, Real data results of Kirchhoff elastic wave migration: *Geophysics*, **51**, 1006–1011.
- Geoltrain, A., and Brac, J., 1993, Can we image complex structures with first-arrival traveltime?: *Geophysics*, **58**, 564–575.
- Grant, F. S., and West, G. F., 1965, Interpretation theory in applied geophysics: McGraw-Hill.
- Kelly, K. R., 1983, Numerical study of Love wave propagation: *Geophysics*, **48**, 833–853.
- Kelly, K. R., Ward, R. W., Treitel, S., and Alford, R. M., 1976, Synthetic seismograms: A finite difference approach: *Geophysics*, **41**, 2–27.
- Kuo, J. T., and Dai, T. F., 1984, Kirchhoff elastic wave migration for the case of noncoincident source and receiver: *Geophysics*, **49**, 1223–1238.
- Loewenthal, D., Stoffa, P. L., and Faria, E. L., 1987, Suppressing the unwanted reflections of the full wave equation: *Geophysics*, **57**, 1007–1012.
- McMechan, G. A., 1983, Migration by extrapolation of time-dependent boundary values: *Geophys. Prosp.*, **31**, 412–420.
- McMechan, G. A., and Sun, R., 1991, Depth-filtering of first breaks and ground roll: *Geophysics*, **56**, 390–396.
- Mittet, R., 1994, Implementation of the Kirchhoff integral for elastic waves in staggered-grid modeling schemes: *Geophysics*, **59**, 1894–1901.
- Mufti, R. M., Pita, J. A., and Huntley, R. W., 1996, Finite difference depth migration of exploration-scale 3-D seismic data: *Geophysics*, **61**, 776–794.
- Rutherford, S. R., and Williams, R. H., 1989, Amplitude-versus-offset variations in gas sands: *Geophysics*, **54**, 680–688.
- Sheriff, R. E., and Geldart, L. P., 1982, Exploration seismology v. 1, History, theory, and data acquisition: Cambridge Univ. Press.
- Sun, R., 1999, Separating  $P$ - and  $S$ -waves in a prestack 2-dimensional elastic seismogram: 61th Ann. Mtg., Eur. Assn. Geosci. Eng., Extended Abstracts, paper 6-23.
- Sun, R., Chow, J., and Chen, K. J., 2001, Phase correction in separating  $P$ - and  $S$ -waves in elastic data: *Geophysics*, **66**, 1515–1518, this issue.
- Sun, R., and McMechan, G. A., 1986, Prestack reverse-time migration for elastic waves with application to synthetic offset vertical seismic profiles: *Proc. IEEE*, **74**, 457–465.
- , 1991, Depth-filtering for one-component seismic data: *Geophysics*, **56**, 1482–1485.

#### APPENDIX A CORRECTING S-IMAGE POLARITY

The  $S$ -image polarity reversal (Figure 4b) originates at the reflection point (at which  $P$ -to- $S$  conversion occurs). The polarity to either side of the source (at  $x=2.0$  km) is reversed (e.g., Balch and Erdemir, 1994). The origin of the  $S$ -wave polarity reversal is illustrated using the reflection of a  $P$ -wave, emitted from an outgoing  $P$ -wave source, at the dipping reflector in Figure A-1. A  $P$ -wave has longitudinal particle motion, whereas an  $S$ -wave has transverse particle motion. The incident  $P$ -wave starts with particle motion of positive (+)  $z$ -component (arrows  $P_{iA}$ ,  $P_{iO}$ , and  $P_{iB}$ ). The reflected  $S$ -wave recorded at the source location is reflected at normal incidence at point  $O'$  and has zero amplitude (see Figure 3b) because incident  $P$ -wave provides zero transverse particle motion (parallel to the reflector). The  $S$ -wave recorded at point A (to the left of the source) is reflected at a point  $A'$  where the incident  $P$ -wave has starting particle motion (arrow  $P_{iA}$ ) with a negative ( $\ominus$ )  $x'$ -component. The reflected  $S$ -wave thus starts with particle motion (arrow  $S_{rA}$ ) with a negative  $x'$ -component, and arrives at the earth's surface with a negative  $x$ -component (arrow A). Similarly, the reflected  $S$ -wave recorded at point B (to the right of the source) arrives with particle motion (arrow B) of positive  $x$ -component (Aki and Richards, 1980). Thus, particle motion directivity to either side of the source is reversed. This is the origin of the polarity reversal in the  $P$ -to- $S$  converted waves (Balch and Erdemir, 1994).

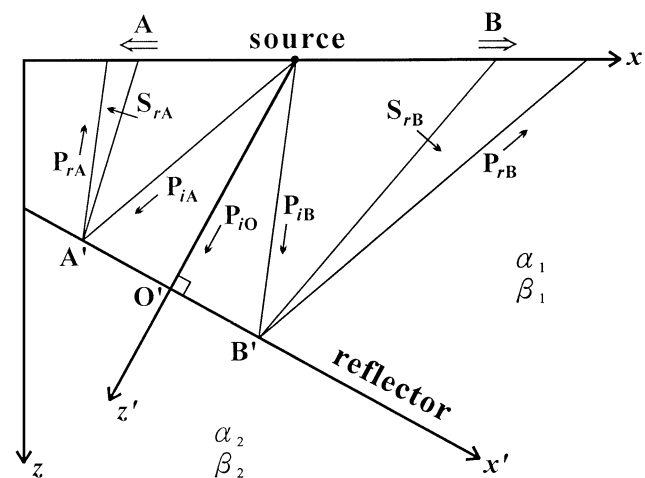


FIG. A-1. Polarization of reflected waves illustrating the origin of  $S$ -wave polarity reversal at zero offset. An outgoing  $P$ -wave source is assumed.  $\phi_1$  and  $\phi_2$  ( $\phi_1 \neq \phi_2$ ) are  $P$ -velocities;  $\phi_1$  and  $\phi_2$  ( $\phi_1 \neq \phi_2$ ) are  $S$ -velocities.  $P_{iA}$ ,  $P_{iO}$ , and  $P_{iB}$  are incident  $P$ -waves at points  $A'$ ,  $O'$ , and  $B'$ . Similarly,  $P_{rA}$  and  $P_{rB}$  are reflected  $P$ -waves and  $S_{rA}$  and  $S_{rB}$  are reflected (converted)  $S$ -waves. The single-tailed arrows denote the particle motions, and the double-tailed arrows denote the  $x$ -components of the particle motions due to the converted  $S$ -wave reflections.



The source (zero offset) point (with zero amplitude) is a node between reversed polarities in the  $P$ -to- $S$  converted reflections, even for those that originate at dipping reflectors (see Figure 10b). This polarity reversal can be corrected simply by multiplying the  $S$ -wave amplitudes by  $\pm 1$  in the region to the left of the source after  $P$ - $S$  wave separation. If the  $P$ -velocity to  $S$ -velocity ratio varies from place to place so the downgoing normal incidence ( $P$ -wave) and the upgoing converted ( $S$ -wave) path are not the same, the polarity change may not be exactly at zero offset, but will be close to it. Since the  $P$ -to- $S$  converted amplitudes are very small in this region, the error introduced by an uncertainty in the position of the

node into the polarity correction will be modest and can be tolerated.

The  $S$ -wave polarity correction is applied to the  $S$ -wave extracted at some depth  $z_1$  with the source location being the node between reversed polarities. This assumption is always valid if the medium is laterally homogeneous. For a laterally inhomogeneous medium, however, it is absolutely valid only if  $z_1$  is the same as the source depth because the ray path of the normal incidence is not vertical. It will remain approximately valid only if  $z_1$  is close to the source depth, as is done for the model in Figure 8. A choice of  $z_1$  too much different from the source depth will be unacceptable.